33rd Symposium on Naval Hydrodynamics
Osaka, Japan, 18 October - 23 October 2020

Large eddy simulation for the investigation of different regimes of cavitation

F. L. Brandao[1], A. Madabhushi[1], M. Bhatt[1] and K. Mahesh[1]
([1]Aerospace Engineering and Mechanics, University of Minnesota, USA)

ABSTRACT

Cavitation is investigated over a range of regimes from inception to developed cavitation for various flow configurations. Cavitation inception is investigated for two configurations; shear layer of a backward–facing step and vortex pair interaction. Flow over a backward–facing step is simulated at $Re_\tau = 800$ and inception is observed in streamwise vortices in the shear layer. Interaction of the counter–rotating vortex pair is studied at $Re = 2 \times 10^5$ and the mechanism for inception is explained as a three–phase process. The developed cavitation regimes are investigated for two configurations; a sharp wedge and a circular cylinder. Flow over a sharp wedge is studied in the experimental configuration of Ganesh et al. (2016). Physical mechanisms of cavity transition observed in the experiments; i.e. re–entrant jet and bubbly shock waves, are both captured in the LES. In addition, very good comparison to the experiments is observed on several fronts; vapor volume fractions, shock speed and shedding frequency. Cavitating flow over a circular cylinder is investigated for cyclic, transitional and non–cavitating regimes. Dynamic mode decomposition (DMD) is used to investigate wake characteristics at $Re = 200$. At $Re = 3900$, vorticity production is analysed and is found to decrease with cavitation number reduction.

INTRODUCTION

Cavitation in marine applications (e.g. marine propellers, hydrofoils) exists over different regimes – ranging from inception to massive regions of vapor. Cavitation over marine propellers is shown as an illustration in figure 1.

Cavitation inception is commonly observed in the turbulent shear layers, tip vortices and wakes of marine geometries (e.g. hydrofoils, propeller blades etc). Tip vortex cavitation has been widely studied (Arndt, 2002) and it mainly occurs when the base (static) pressure of the tip vortex core drops below the vapor pressure. Inception in regions where multiple vortices interact (wake of hydrofoils, propellers blades etc.) is a relatively less explored area. Interestingly, in such flows, the vortices whose strength is much less than the neighboring vortices are often observed to incept first. For example, in turbulent shear layers, depending upon the flow conditions cavitation inception can often be observed in quasi streamwise vortices at higher ambient pressures as compared to stronger spanwise vortices (O'Hern, 1990). To study inception in such complicated flows, it is essential to understand interaction between unequal strength vortices through canonical problems. One such experimental study was done by Chang et al. (2012) for flow over a pair of hydrofoils. Vortex pair of different strengths was generated downstream of the hydrofoils by varying the angle of attack and weaker vortex was observed to incept first for certain cases. Core stretching is one of the two factors causing a drop in its pressure and the other factor was hypothesized to be generation of axial jet in the core.

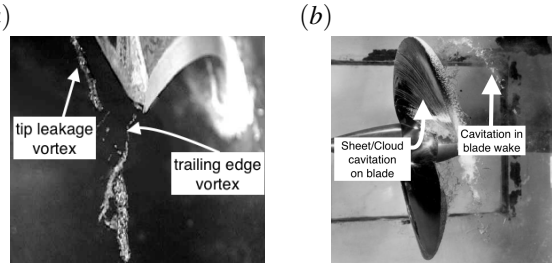

Figure 1: Propeller cavitation. (a) Cavitation inception due to interacting tip leakage and trailing edge vortices (Chesnakas and Jessup, 2003). (b) Massive sheet/cloud cavitation (Mitchell et al., 2013).

With the reduction in cavitation number ($\sigma = 2(p_\infty - p_v)/\rho U_\infty$), vapor regions grow in size forming large sheet like structures on the suction side of the body. The transition of this sheet cavity into to the cloud is referred as "sheet to cloud". The sheet to cloud transition depends on the geometry of the body, cavitation number, confinement etc. Re–entrant jet and bubbly shock waves have been shown as instability mechanisms

for the transition (Callenaere et al., 2001; Ganesh et al., 2016). For bluff–bodies, vapor is formed inside the low pressure region of a vortex core and is shed along with it. As σ is reduced further, the cavities grow in size and the passage of a bubbly shock dominates the shedding mechanism. This behavior has been observed in flows over different configurations like: wedge (Ganesh et al., 2016), hydrofoil (Bhatt et al., 2018), cylinder (Brandao et al., 2020) and triangular prism (Ganesh et al., 2018).

The present study is aimed at investigating cavitation over a range of regimes. Cavitation inception is studied for flow over a backward-facing step and for unequal strength vortex pair interactions. Developed cavitation is studied using a sharp wedge and a circular cylinder configurations. The paper is organized as follows. First, we describe the governing equations, physical model and numerical method. This is followed by a discussion of the problem setup for each configuration. The results for each problem are then discussed. The paper concludes with a brief summary.

CAVITATION INCEPTION

Numerical method

Incompressible Navier–Stokes equations are solved for the problems concerning inception - LES of shear layer and DNS of a vortex pair interaction. The unfiltered equations are given by

$$\frac{\partial u_i}{\partial x_i} = 0 \tag{1}$$

$$\frac{\partial u_i}{\partial t} + u_j \frac{\partial u_i}{\partial x_j} = -\frac{\partial p}{\partial x_i} + \nu \frac{\partial^2 u_i}{\partial x^2}. \tag{2}$$

These equations are solved using a finite-volume algorithm developed by Mahesh et al. (2004) which ensures robustness without any added numerical dissipation. This algorithm has been validated for a variety of problems. It is based on a predictor–corrector approach. The Cartesian velocities (u_i) and pressure (p) are stored at cell centers and the face normal velocities are stored at the center of the faces. The velocities are first predicted at cell centers and then interpolated to obtain the face–normal velocities. The face–normal velocity is projected to discretely satisfy the continuity equation. This yields a pressure Poisson equation which is solved using a multi–grid approach and then the pressure gradients ($\frac{\partial p}{\partial n}$) are obtained using a least–squares formulation. Finally, these pressure gradients are used to correct the velocities at cell centers. Implicit time advancement is performed using the Crank–Nicolson scheme. For the study of inception in a backstep configuration, we treat vapor as a passive scalar. The main idea is that since inception is a stochastic process that generates small amounts of vapor for short periods of time, the effects of these small regions of vapor on the flow dynamics and liquid density are negligible. The algorithm is based on the work of Muppidi and Mahesh (2008) for passive scalar in jets. The transport equation for the passive scalar is given in equation 3. Here, the passive scalar is taken as the concentration of vapor, $C = \rho Y_v$, and the cavitation source terms are obtained from Saito et al. (2007). The volume fraction of vapor can be obtained by dividing its concentration by the vapor density, $\alpha_v = \rho Y_v / \rho_v$. The Schmidt number for vapor in water is $Sc = 500$ and ρ is the mixture density, which is assumed constant. Here, it is important to mention that the Dynamic Smagorinsky model (DSM) is employed for the momentum and continuity equation only and DNS is done for the transport equation of a passive scalar. Addition of subgrid models for the passive scalar is under development.

$$\frac{\partial C}{\partial x_i} + \frac{\partial C u_j}{\partial x_j} - \frac{\nu}{Sc} \frac{\partial^2 C}{\partial x_j^2} = S_e - S_c \tag{3}$$

a) Inception in shear layer

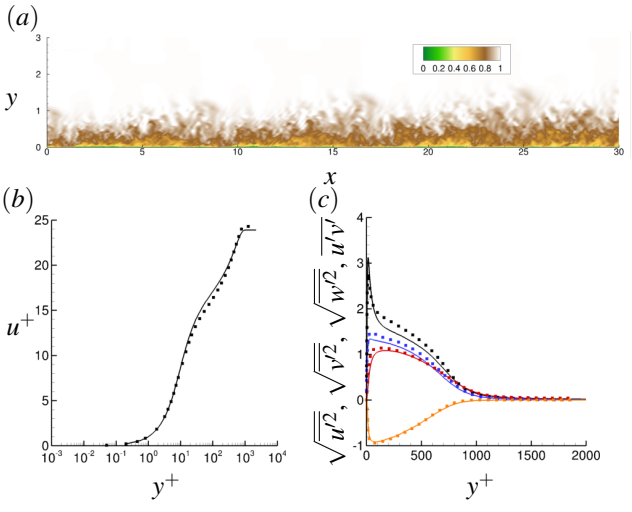

Figure 2: Turbulent boundary layer colored by axial velocity (a). Mean values of axial velocity (b) and values of Reynolds stresses (c) at $Re_\tau = 800$. Simulation results (lines) compared against data from Schlatter and Örlü (2010) (symbols). Black, red, blue and orange lines and symbols in (c) represent, respectively, $\sqrt{\overline{u'^2}}$, $\sqrt{\overline{v'^2}}$, $\sqrt{\overline{w'^2}}$ and $\overline{u'v'}$.

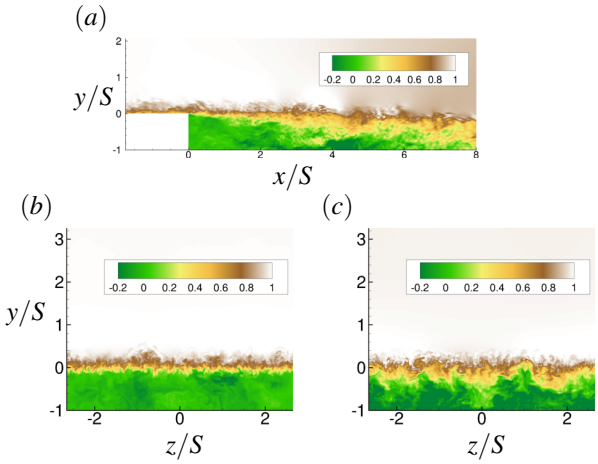

Figure 3: Instantaneous flow field at center plane (a) and at positions $x = 1S$ (b) and $x = 3S$ (c) downstream of the step. S represents the step height.

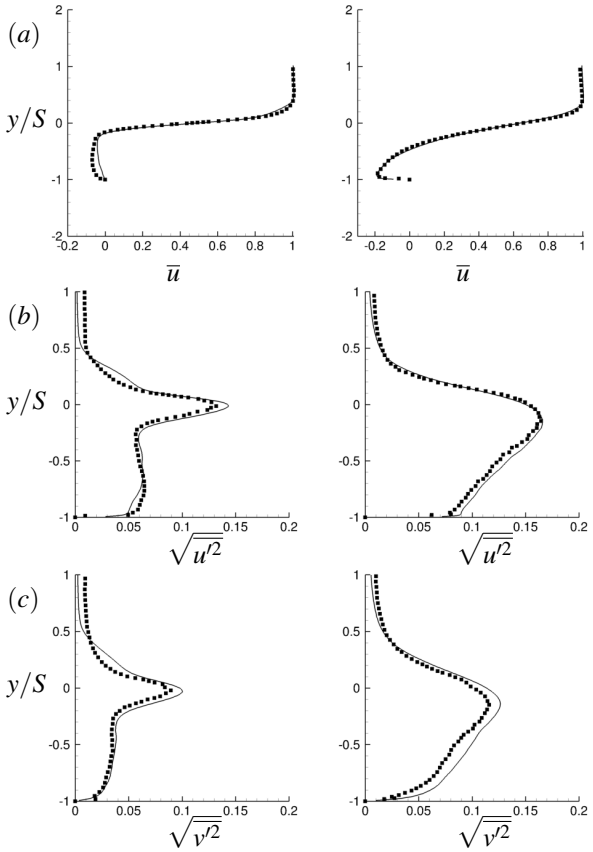

Figure 4: Comparison between numerical (lines) and experimental (symbols) velocity profiles at $x = 1S$ (left) and $x = 3S$ (right) downstream of the step. S represents the step height.

Inception in shear layers is studied using the backstep configuration with step height of $S = 10mm$ of Agarwal et al. (2018) at $Re_\tau = 800$. A turbulent boundary layer is generated on a separated plane through the recycle–rescale method of Lund et al. (1998), later extended to unstructured grids by Kumar and Mahesh (2016), and used as an inflow boundary condition for the backstep. The work of Agarwal et al. (2018) studies different values of σ, but does not observe inception for $Re_\tau = 800$. Thus, in the present work we have reduced σ to values below those employed by Agarwal et al. (2018), until

cavitating structures became considerable and hence $\sigma = 0.25$. The computational mesh has approximately 127 million cells and the proximity of the corner is refined with $\Delta y^+ = 0.38$ and $\Delta x^+ = 20$. Grid size is uniform in spanwise direction with $\Delta z^+ = 10$. The grid was chosen based on the value of u_τ obtained in the boundary layer simulation. No grid refinement study was necessary since the following results obtained with this mesh already provided good comparison.

Results

In order to obtain the same condition as the experiments in the shear layer, we must first obtain the correct behavior of the incoming turbulent boundary–layer. This turbulent boundary–layer is generated on a separated flat plane following the procedure in Lund et al. (1998) and validated against the data of Schlatter and Örlü (2010). Figure 2 shows the boundary–layer colored by axial velocity and its validation at $Re_\tau = 800$. This boundary–layer is then used as an inflow for the backstep. Figure 3 shows the instantaneous flow field in the center plane and at different positions downstream of the step. The flow separating at the step corner and forming a recirculating region can be observed. Velocity profiles at some locations downstream of the step are displayed in figure 4 and show very good agreement with experimental data of Agarwal et al. (2018).

Figure 5(a) shows isosurfaces of Q–criterion. Observe the presence of an elongated vortical structure in the axial direction, indicated by the arrow, at a random location in the shear layer. From figure 5(b), it becomes evident that the instantaneous small values of pressure are scattered throughout vortical structures in the shear layer, as expected. More specifically, it can be observed that the lowest value belongs to the elongated axial vortex indicated by the arrow. Figure 5(c) confirms that this structure cavitates first. This agrees well with the behavior observed experimentally (O'Hern, 1990; Agarwal et al., 2018).

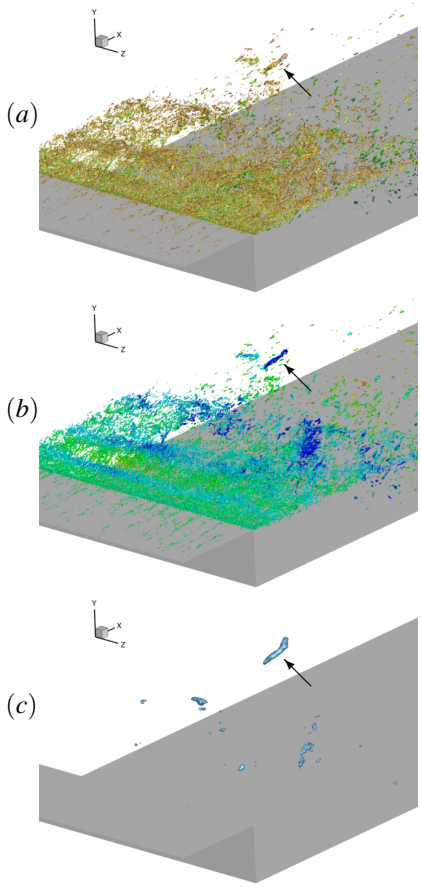

Figure 5: Q–criterion colored by axial velocity (a) and pressure (b). Isosurface of $\alpha_v = 0.1$ showing inception in streamwise vortical structure (c). The arrow indicates the cavitating streamwise vortex. Flow is in the positive x–axis.

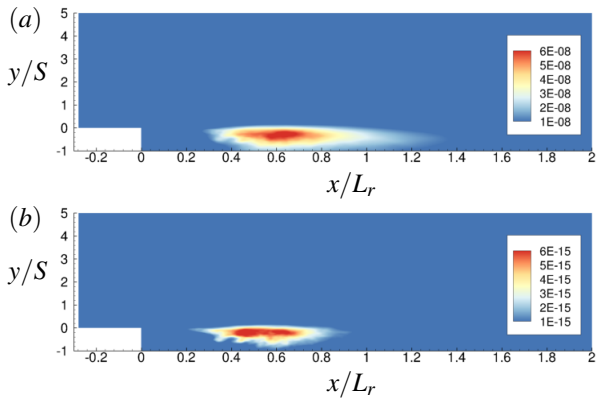

Figure 6: Mean (a) and fluctuation (b) values of vapor mass fraction for $Re_\tau = 800$. The x–axis is non–dimensionalized with the reattachment length.

Figure 6 shows mean and fluctuation values of vapor mass fraction. It can be observed that the peak values are very small, indicating inception and that the changes in the liquid density are negligible. Although inception is not observed experimentally at $Re_\tau = 800$, the work of Agarwal et al. (2018) reports that at different higher Re_τ and at different σ, the location where inception is most likely to occur is at $0.45 < x/Lr < 0.75$. In our simulation, figure 6 reveals that cavitation is active at around $0.4 < x/Lr < 0.8$ along the shear layer, showing good agreement with the experiments.

b) Vortex pair interaction

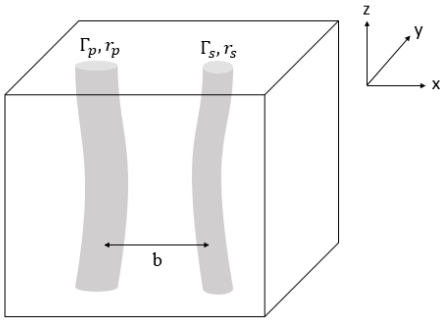

Figure 7: Setup for the vortex pair interaction.

The setup consists of two unequal strength counter–rotating Lamb–Oseen vortex columns of circulation strengths Γ_p and Γ_s and radii r_p and r_s respectively with axis along z (where p - Primary, s - Secondary). Periodic boundary conditions are used along z axis and Neumann boundary conditions are used in x and y directions which account for $\Gamma_{net} \neq 0$ in the entire domain. The domain size used is $-8b \leq x,y \leq 6b$, where b is the unperturbed distance between the vortex centers. The domain length along z and the initial perturbations on each column in the $x-y$ plane are obtained from the linear theory discussed in Leweke et al. (2016). The mesh is finer in the inner region ($-3.5b \leq x,y \leq 1.5b$) and is stretched in the outer region. 32 cells are used to discretize the smaller core radius (grid convergence established). The time step convergence has been established and the non-dimensional time step used for the current simulation is $\Delta t = 2.5e^{-4}$ (non-dimensionalization based on the reference distance (b) and the reference velocity ($\Gamma/2\pi b$)). The parametric setup used is same as Case 1 of Chang et al. (2012).

$$\Gamma = \frac{\Gamma_s}{\Gamma_p} = -0.25, \quad \frac{r_s}{b} = 0.176$$
$$\frac{r_p}{b} = 0.286, \quad Re_{\Gamma_p} = 200,000 \tag{4}$$

Results

To understand inception during a vortex–pair interaction where the base pressure of each core is much higher than the vapor pressure, it is essential to understand the factors responsible for causing changes in the core pressure and other core properties such as its shape, size, vorticity etc. It is known that inception in such cases generally occurs during the later stages of interaction when the cores are very close to each other (Chang et al., 2012). Hence the investigation of the later stages of evolution i.e. the non-linear regime is the focus of this section. The non–linear regime can be broken down into three phases. Phase A is mostly governed by the changes in the secondary core properties whereas in phase B the primary core undergoes significant changes in its shape and size. In Phase C, both the cores completely break–up i.e., they undergo drastic changes.

Phase A:

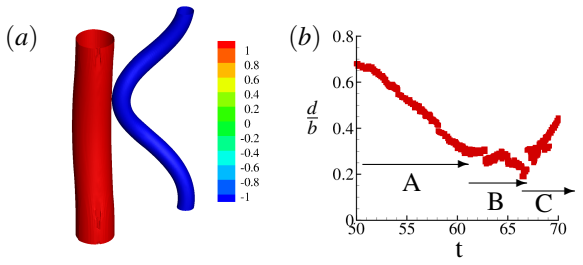

Figure 8: (a) Q–criterion plots of the vortex filaments colored with ω_z (blue – secondary, red – primary), (b) Distance between the core centers normalized w.r.t the initial separation b.

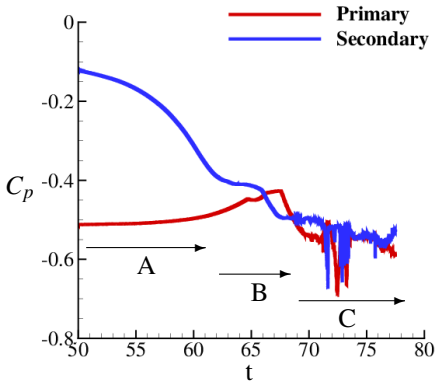

Figure 9: Minimum pressure in the secondary core and the primary core.

Prior to Phase A, the secondary core develops large curvature while the primary core remains almost columnar (Figure 8(a)). This is because of the large strength difference between the filaments i.e. the strain exerted by the secondary core is not sufficient to deform the primary core. From the Biot–Savart law it can be intuitively understood that a large curvature causes a large self–induced velocity pushing the secondary core towards the primary core at a faster rate. This can be seen in Figure 8(b) where the distance between the core centers reduces sharply in this phase. The minimum pressure in both cores is tracked separately and this is shown in Figure 9. It can be seen that the secondary core pressure (blue curve) decreases and also, significant reduction in its size is observed (Figure 10). These changes in the secondary core's size and pressure are seen to be

$$\frac{C_p(t\sim 60)}{C_{po}} \sim 4, \quad \frac{r(t\sim 60)}{r_o} \sim 0.5 \tag{5}$$

where t is the non-dimensional time (non-dimensionalized with $\frac{\Gamma_p}{b^2}$), C_{po} and r_0 are the unperturbed secondary core pressure and size respectively. The pressure behavior follows the Euler–n equation for a single vortex filament.

$$C_p(t) \propto \frac{\Gamma}{r(t)^2} \tag{6}$$

The shape of the secondary core initially transforms from circular to elliptical due to the higher strain exerted by the primary core (seen in Figure 10(a)). The stretching of the secondary filament causes its size to decrease and its vorticity to increase. As a result, it exerts a large strain on the primary core and hence the primary core's shape flattens (Figure 10(c)). Since there is no significant change in the primary core's size, its pressure and vorticity mostly remain unchanged during this phase (Figure 9).

Phase B:

As the cores approach close to each other at the end of phase A, the secondary core's velocity due to mutual strain will be large and more dominant than its self-induced velocity. This results in both the cores rotating in almost concentric circular paths. Hence, the distance between the core centers is almost constant (Figure 8(b)). Also, the dominance of the mutual strain leads to reduced stretching rate of the secondary filament. This causes a smaller reduction in the secondary core's pressure and size (pressure reduces by 20% approximately (Figure 9) and its size reduces by 10%). These changes in the core pressure and core size still follow the Euler–n equation discussed in the previous section. Also, it is important to distinguish the behavior of the vortex cores in this phase for lower and higher Re. For low Re ($O(10^3)$), the high vorticity gradients coupled with high viscosity lead to rapid decay in the circulation of each of the cores (Marshall et al. (2001)). This would in turn decrease the core vorticity and increase

the core pressure making inception difficult. But for high Re flows ($O(10^5)$), the large viscous diffusion time scales keep the circulation of each core unchanged during this phase; hence preserving the high core vorticity and low core pressure.

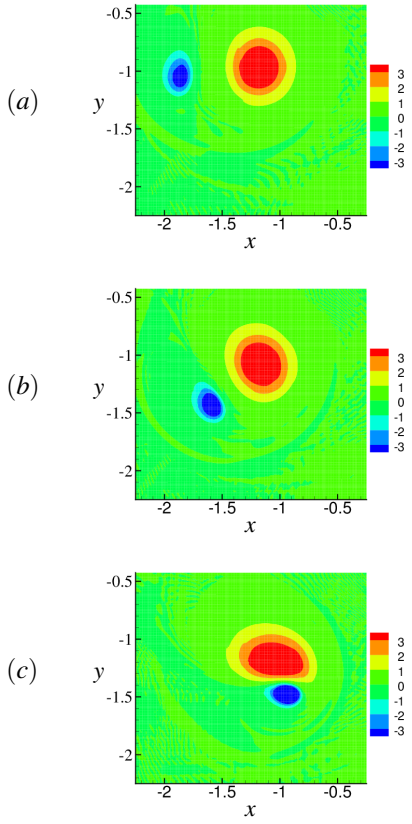

Figure 10: Axial vorticity (ω_z) contour plots in the closest plane of approach ($z = 0$) during phase A at (a) T = 50, (b) T = 55 and (c) T = 60.

The secondary filament's stretching in this phase results in further increase in its vorticity. Hence it exerts higher strain on the primary core resulting in further deformation of the primary core's shape (Figure 11(a)). The primary filament's negligible stretching coupled with its core shape deformation results in its core pressure to increase during this phase (Figure 9).

Phase C:

In this phase both the cores eventually breakup. At the end of phase B (Figure 11(b)), it can be seen that a sheet like structure is developed at the top of the primary core due to the strong strain imposed by the secondary core. This sheet continues to get stretched, and it wraps around the secondary core. During this stretching process, the sheet's vorticity and strain increase thus imposing higher strain on the periphery of the nearby secondary core. Moore and Saffman (1971) have analytically studied the effect of uniform irrotational strain on a Rankine vortex and have established that the core becomes unstable and can breakup for $\varepsilon(S/\omega) > 0.15$. But for a core with non-uniform vorticity, this stability is a local behavior i.e. it would depend on the local ε (Hurst et al., 2018). For the current simulations where the vorticity has an axisymmetric Gaussian profile, the periphery of the core starts to break up first as it has lower vorticity compared to the core center (Figure 12(b)). This process would proceed towards the core center and the entire core would break up leaving behind a region of small scale structures.

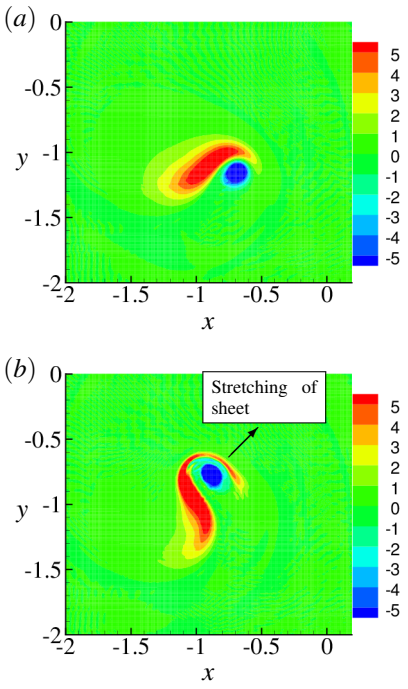

Figure 11: Contour plots of vorticity (ω_z) in the closest plane of approach (z = 0) during phase B displaying the flattening process of primary core at (a) T = 62.5 and (b) T = 65.

The pressure minima ($C_{p_{min}}(t)$) for both the cores occur during this phase (Figure 9). Figure 13(a) shows the variation of $C_p(t)$ and the corresponding axial velocity (w) and Figure 13(b) shows the variation of $C_p(t)$ and the corresponding axial vorticity (ω_z) for the secondary core. Preliminary observations reveal $C_{p_{min}}(t)$ occuring at two different instants of time. At $t \sim 71.6$ a small axial velocity can be seen (Figure 13(a)) and huge increase in vorticity (Figure 13(b)) can be observed. This axial jet is not sufficient to produce the observed drop in pressure. This probably could mean a strong local stretching of the small scale structures occurs causing a sharp spike in vorticity and resulting in a sharp drop

in pressure. Soon, the pressure recovers to a value of -0.5 and a second dip is observed at $t \sim 73$. At this instance, a strong axial jet is observed. Pressure reduction due to generation of axial jets during such vortex pair interactions was hypothesized by Chang et al. (2012). Such mechanism could serve as explanation in the present study. However, further investigation is required to ascertain the relationship between the axial jets and corresponding drop in pressure, and to establish the source of such axial jets and local stretching of the unorganized small–scale vorticity structures.

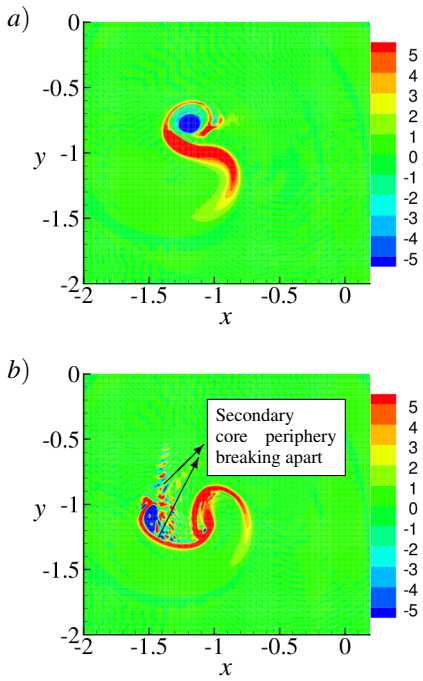

Figure 12: Contour plots of axial vorticity (ω_z) in the closest plane of approach (z = 0) in phase C displaying the breaking up process at *a*) T = 67.5 and *b*) T = 70.

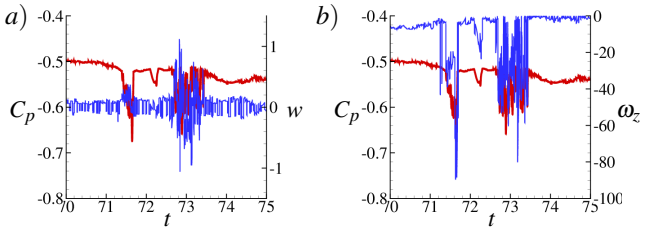

Figure 13: *a*) Variation of C_p(red) and corresponding axial velocity w (blue) for the secondary core. *b*) Variation of C_p(red) and corresponding axial vorticity ω_z(blue) for the secondary core.

DEVELOPED CAVITATION

Numerical method

Developed cavitation is studied using the homogeneous mixture model. In the homogeneous mixture model, the mixture of water, vapor and non–condensable gas (NCG) is treated as a single compressible fluid. The mixture is assumed to be in thermodynamic and mechanical equilibrium among its constituent phases. The governing equations are the compressible Navier–Stokes equations solved for mixture quantities along with the transport equation for vapor mass transfer employing finite rate mass transfer between the phases. The equations are spatially Favre filtered for LES and given as;

$$
\begin{aligned}
\frac{\partial \overline{\rho}}{\partial t} &= -\frac{\partial}{\partial x_k}\left(\overline{\rho}\tilde{u_k}\right), \\
\frac{\partial \overline{\rho}\tilde{u_i}}{\partial t} &= -\frac{\partial}{\partial x_k}\left(\overline{\rho}\tilde{u_i}\tilde{u_k} + \overline{p}\delta_{ik} - \tilde{\sigma}_{ik} - \tau_{ik}\right), \\
\frac{\partial \overline{\rho}\tilde{Y_v}}{\partial t} &= -\frac{\partial}{\partial x_k}\left(\overline{\rho}\tilde{Y_v}\tilde{u_k} - t_k\right) + \tilde{S_e} - \tilde{S_c} \\
\frac{\partial \overline{\rho}\tilde{Y_g}}{\partial t} &= -\frac{\partial}{\partial x_k}\left(\overline{\rho}\tilde{Y_g}\tilde{u_k} - t_k\right) \quad \textit{and} \\
\frac{\partial \overline{\rho}\tilde{e_s}}{\partial t} &= -\frac{\partial}{\partial x_k}\left(\overline{\rho}\tilde{e_s}\tilde{u_k} - \tilde{Q}_k - q_k\right) \\
&\quad - \overline{p}\frac{\partial \tilde{u_k}}{\partial x_k} + \tilde{\sigma_{ik}}\frac{\partial \tilde{u_i}}{\partial x_k}.
\end{aligned}
\tag{7}
$$

Here, the tilde quantities are Favre averaged quantities and τ_{ik}, q_k and t_k are subgrid scale (SGS) terms namely: SGS stress, SGS heat flux and SGS scalar flux. These terms are modeled using the Dynamic Smagorinsky model (DSM) (Moin et al., 1991). ρ, u_i, e_s and p are density, velocity, internal energy and pressure respectively, of the mixture. Y_v is the vapor mass fraction and Y_g is the NCG mass fraction. σ_{ij} and Q_k are the viscous stress tensor and the heat flux vector respectively. S_e and S_c are evaporation and condensation source terms given by Saito et al. (2007).

The system is closed by a non–barotropic mixture equation of state given by the stiffened equation of state in water and ideal gas equation of states in both vapor and NCG. The speed of sound of the mixture is derived from the mixture equation of state and the Gibbs equation, which compares well with measured frozen sound speed in literature (Brandao et al., 2020).

The numerical method is based on a predictor–corrector approach, where the predictor step uses non–dissipative finite volume scheme and corrector step uses a characteristic based filter in the vicinity of discontinuities. Time integration is performed by the explicit Adams–Bashforth method. A detailed description of physical modeling and numerical methodology are

given in Gnanaskandan and Mahesh (2015). The methodology is extended to include NCG by Brandao et al. (2020).

a) Sheet to cloud transition

Sheet to cloud cavitation over a wedge is simulated using compressible homogeneous mixture approach with LES. The inflow/outflow conditions of the experimental sharp wedge configuration (Ganesh et al., 2016) is matched to study diverse cavitation regimes in the computations. The details are given in Bhatt and Mahesh (2020). Here, only the developed cavitation in the transitory and periodic regimes is discussed. The computational mesh consists of approximately 3 million hexahederal cells. The mesh is refined in the convergent–divergent section of the wedge with minimum spacing of $0.005h$ ($\sim 0.125\ mm$) in both the stream–wise and the wall–normal directions. Here h $(1\ inch)$ is the wedge height. The boundary-layer refinement is not considered for the top and the side walls, since it allows significant reduction in the mesh-size without affecting the overall confinement. Also, the relevant flow features are expected to be in the vicinity of the bottom-wall. For the bottom-wall, the normal spacing of $0.005h$ is chosen to sufficiently capture the re-entrant jet. Also, the incoming boundary layer profiles at the bottom-wall are compared to the experimental measurements of Ganesh et al. (2016), see Bhatt and Mahesh (2020) for the details. The flow is simulated at Reynolds number $Re = \frac{\rho_\infty u_\infty h}{\mu_\infty} = 203000$, where the subscript '$\infty$' represents free stream values. Back cavitation number σ_b is defined as $\sigma_b = \frac{p - p_v(T)}{1/2 \rho_\infty u_I^2}$. Here, u_I is the inflow velocity. σ_b is reduced to progress from the transitory to the periodic regime. Transitory regime is simulated at $\sigma_b = 1.89$ and periodic regime is simulated at $\sigma_b = 1.78$.

Results

Re-entrant jet and bubbly shock waves

We present LES results for transitory and periodic regimes in the flow over a sharp wedge. This section illustrates how LES captures both instability mechanisms; i.e. re–entrant jet and bubbly shock waves, in these developed cavitation regimes. Figure 14 shows the instantaneous solution using LES at $\sigma_b = 1.89$. Note the liquid re–entrant jet at the mid–cavity (figure 14(b)). Intermittent nature of pressure waves and mid-cavity detachment of sheet cavity into the cloud is visualized in figure 14(a). $\langle \alpha_v \rangle$ within the cavity remains in the range ~ 0.4–0.6 and vapor production is observed intermittently inside the cavity and shear layer. With reduction in σ_b, the sheet to cloud transition exhibits periodic behavior. We consider periodic shedding at $\sigma_b = 1.78$. Figure 15 shows an instant of cavity retraction. Bubbly shock waves are visualized by a void fraction discontinuity in the span-wise averaged vapor volume fractions ($\langle \alpha_v \rangle$) in figure 15(b). High values of $\langle \alpha_v \rangle$ ($\sim$0.8–0.9) are observed inside the entire cavity (also observed in the experiments of Ganesh et al. (2016)). Complete collapse of the vapor cloud and the pressure regions due to the cloud collapse are noticeable on the side plane in figure 15(a).

Comparison to the experiments

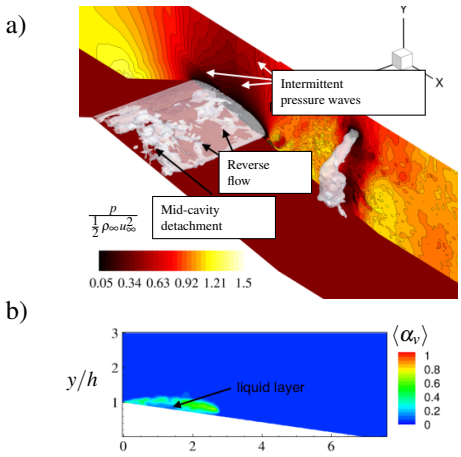

Figure 14: Transitory regime showing re-entrant jet cycle. (a) Iso–contour level $\alpha_v = 0.1$ with pressure plotted on side plane ($x-y$ plane at $z = 2.9h$). (b) Spanwise averaged vapor volume fraction ($\langle \alpha_v \rangle$) for the same instant.

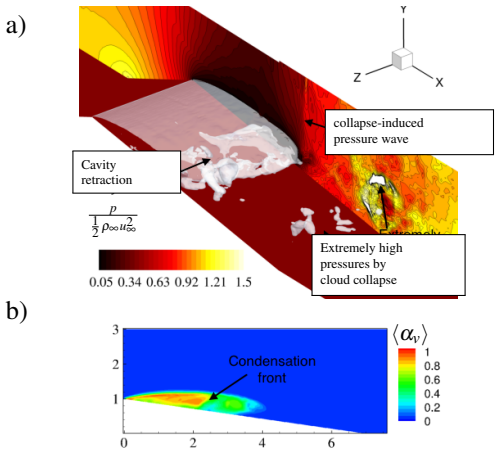

Figure 15: Periodic regime showing bubbly shock cycle. (a) Iso-contour level $\alpha_v = 0.1$ with pressure plotted on side plane ($x-y$ plane at $z = 2.9h$). (b) Spanwise averaged vapor volume fraction ($\langle \alpha_v \rangle$) for the same instant.

We compare the mean volume fraction data to the

X-ray measurements of (Ganesh et al., 2016). In addition, we consider the time evolution of instantaneous vapor volume fraction, condensation front speed and the frequency of periodic shedding for comparison to the experimental data. The mean vapor volume fraction is compared to experiments in figures 16 and 17 for transitory and periodic regimes respectively. For each case, contours of time average of spanwise averaged vapor volume fractions ($\overline{\langle\alpha_v\rangle}$) obtained from LES are plotted alongside the time averaged X-ray measurement data. Here ' $\bar{}$ ' denotes time average. The field of view of the X-ray measurement is matched to LES and contour levels are identical. In addition, profiles of $\overline{\langle\alpha_v\rangle}$ extracted along the y axis from the wedge surface at various axial locations are plotted in figures 16(c) and 17(c). For each case, LES statistics are sampled at $0.005tu_\infty/h$ ($\sim 0.015\ ms$), which provides sufficient temporal resolution to capture variations in cavity size over a given cycle for comparison to the X–ray measurements sampled at 1 ms. Statistics are averaged over approximately 10 shedding cycles (which corresponds to the physical time of $0.5s$ for the periodic shedding case) to capture the low frequency of cloud shedding. Experimental results are taken for total time of $0.79s$, which corresponds to approximately 16 shedding cycle for periodic shedding.

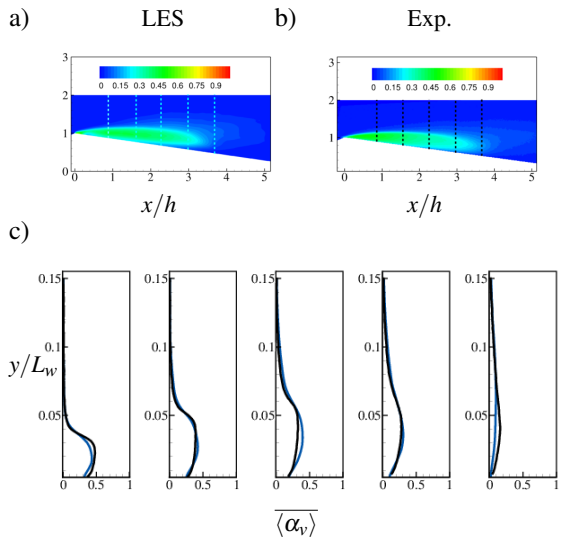

Figure 16: Transitory regime : a) Contours of $\overline{\langle\alpha_v\rangle}$ from LES at $\sigma_b = 1.89$, b) time average of X-ray measurements at $\sigma_b = 1.82 \pm 0.06$ (data obtained from direct communication with H.Ganesh) and c) comparison of the profiles extracted at $s/L_w = 0.1, 0.2, 0.3, 0.4$ and 0.5, indicated by the dashed lines. Black and blue lines respectively indicate experimental and LES profiles.

In both regimes, overall larger regions of vapor are formed (e.g. a sheet cavity of vapor over a wedge surface and cloud shedding downstream). Considering cycle to cycle variation in sheet/cloud cavitation in each regime (also observed in Ganesh et al. (2016)) and the unsteady nature of the flow, the comparison in the overall cavity length and thickness is encouraging. In addition, distribution of vapor volume fraction in the divergent section of the wedge show very good comparison in the free stream, within the cavity and also near the surface of the wedge. This is indicated by $\overline{\langle\alpha_v\rangle}$ profiles in figures 16(c) and 17(c).

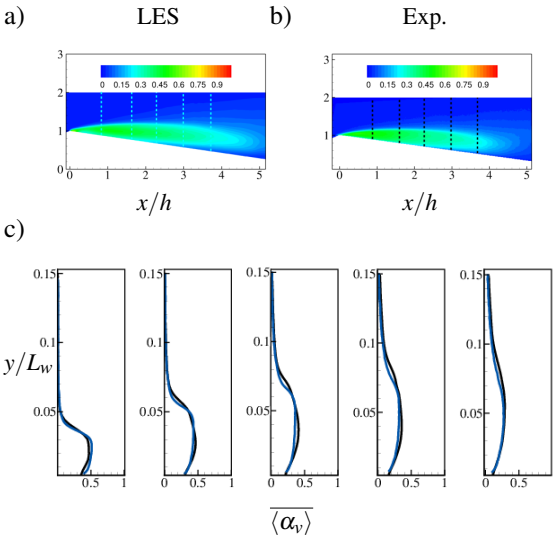

Figure 17: Periodic regime: a) Contours of $\overline{\langle\alpha_v\rangle}$ from LES at $\sigma_b = 1.78$, b) time average of X-ray measurements at $\sigma_b = 1.73 \pm 0.11$ (data obtained from direct communication with H.Ganesh) and c) comparison of the profiles extracted at $s/L_w = 0.1, 0.2, 0.3, 0.4$ and 0.5, indicated by the dashed lines. Black line and blue line respectively indicate experimental and LES profiles.

The frequency of periodic shedding of the cloud at $\sigma_b = 1.784$ is computed from Fast Fourier Transform (FFT) of the time-varying void fraction and pressure signal at $(3h, 1.5h, 1.5h)$ inside the cavity. The signals for the pressure and the void fraction are shown in figures 18(a) and 18(b) respectively. The corresponding FFT is shown in figure 18(c). The signal shows periodic pressure pulses followed by low pressure (vapor pressure $\sim 2\ kPa$) regions spanning approximately 10 cycles taken over 0.5s. FFT of both the signals (α and p) show peaks at identical values of $f = 20.13Hz$, indicating that the cavity shedding mechanism is associated with the propagation of pressure pulses. Shedding frequency of $f = 20.13Hz$ compares very well to the experimental shedding frequency of $f = 20.00Hz$.

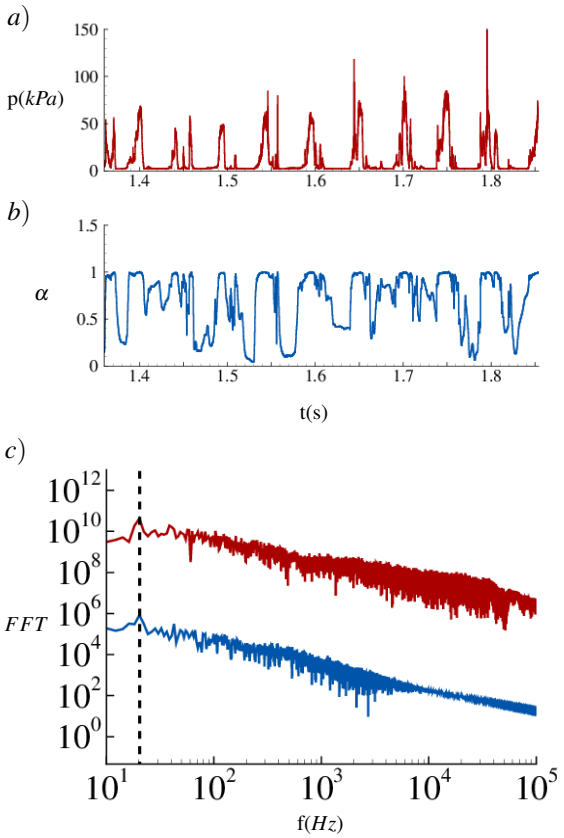

Figure 18: Frequency of shedding. a) p(t), b) $\alpha(t)$ taken at $(3h, 1.5h, 1.5h)$ and c) corresponding FFT (p -, α -).

We construct an $s-t$ diagram to compute the bubbly shock speed. We consider a line parallel to the wedge surface at a normal distance $n = 4$ *mm* and stack the solution for multiple time instances, constructing an $s-t$ diagram. Figure 19 shows time evolution of $\langle\alpha_v\rangle$. The triangular region of $\langle\alpha_v\rangle$ indicates one cycle of cavity shedding. The cavity growth and collapse within the cycle is indicated by white arrows. The slopes of iso-contour lines during cavity growth and retraction can be used to compute the respective speeds. The inverse of the slope in the $s-t$ diagram (figure 19) for cavity retraction indicates bubbly shock speed in the laboratory frame of reference. Bubbly shock speed thus obtained is averaged over 10 shedding cycles for both the experiment and the simulation. The shock speed obtained from LES is 5.0 m/s showing good comparison to the experimental value of 4.5 m/s. The frozen sound speed of this high volume fraction mixture is 3.34 m/s. Mach number computed based on the frozen speed of sound is 1.49. This indicates that the void fraction discontinuity is supersonic and accordingly a "bubbly shock wave". Detailed analyses of the conditions that lead to the formation of re-entrant jet and bubbly shock wave mechanisms using the LES results are provided in Bhatt and Mahesh (2020).

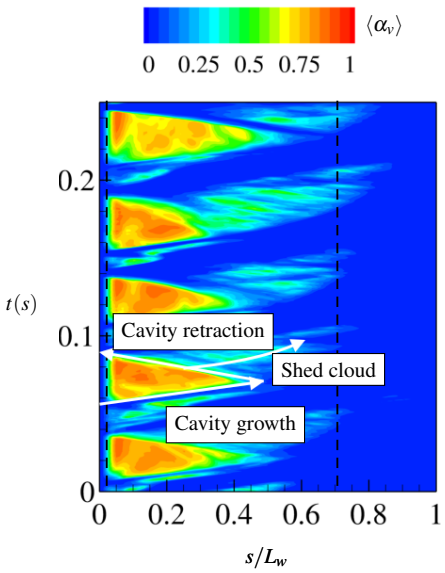

Figure 19: Temporal evolution of $\langle\alpha_v\rangle$ taken on a line parallel to the wedge surface at a normal distance $n = 4$ *mm* for $0.25s$ showing approximately 5 cavity shedding cycles.

b) Flow over a circular cylinder

Cylinder cavitation is simulated for $Re = 200$ and $Re = 3900$ (based on cylinder diameter) at different σ covering cyclic and transitional regimes, as well as a non–cavitating regime. The domain is cylindrical with two– and three–dimensional grids for the laminar and turbulent cases, respectively. The grid and domain size are the same as employed in Brandao et al. (2020): near the cylinder surface both cases use a mesh with spacing 0.005D $\times$ 0.01D in the radial and azimuthal directions respectively, with 80 points being employed in the spanwise direction for the $Re = 3900$ case. Vapor and NCG are uniformly introduced in the free–stream in terms of volume fraction in the quantities of $\alpha_v = 1 \times 10^{-9}$ and $\alpha_g = 1 \times 10^{-6}$, respectively. Acoustically absorbing sponge layers are applied at the boundaries to avoid reflection of pressure waves from the boundaries.

Results

Developed cavitation in flow over cylinder is divided into cyclic and transitional regimes as explained in Brandao et al. (2020). The cyclic regime is characterised by the periodic shedding of the cavitating vortices that originate at the surface and is observed for high values of σ as seen in figure 20(a). These vortices, filled with vapor, collapse as they move downstream producing pressure waves. With the reduction in σ, the flow enters into the transitional regime and the shedding process alternates between two phenomena. The first is similar

to cyclic cavitation, but the vortex cores cavitate further downstream and the cavity formed is not attached to the cylinder, as shown in figure 20(b). During this part of the cycle, the cylinder surface and the near wake remain cavitation free. A second phenomenon follows where the instantaneous pressure in the near wake drops below vapor pressure. A cavity forms in the region symmetrically spanning the entire aft–body of the cylinder, as seen in figure 20(c). The closure region then collapses generating a bubbly shock that travels upstream detaching the cavity. Due to this, the Strouhal number of the shedding frequency of drag time history based on the cylinder diameter ($St = fD/U_\infty$) shows a sharp jump between regimes of one order of magnitude, as visible in figure 21

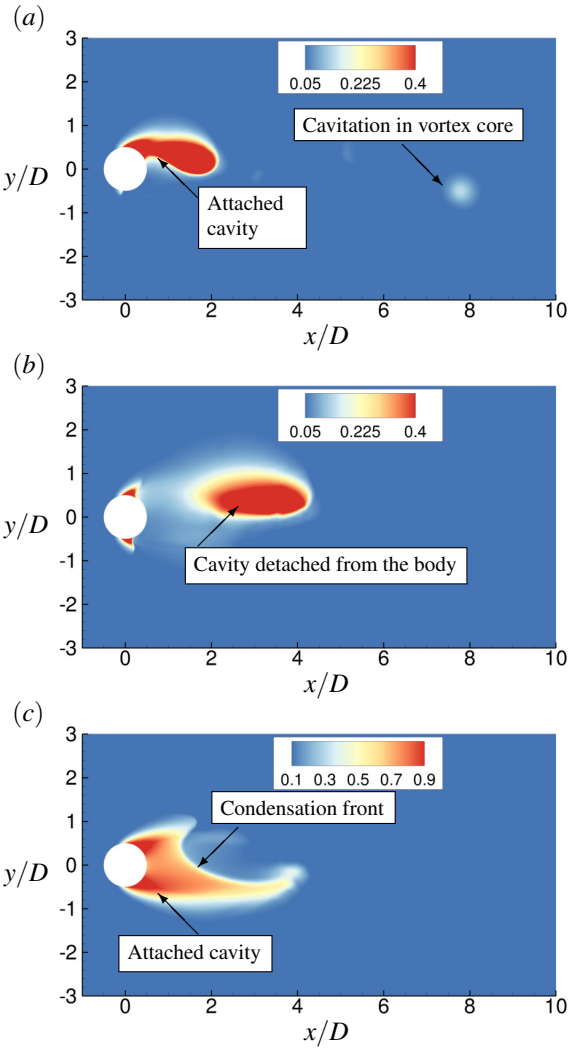

Figure 20: Instantaneous total void fraction contour for the cyclic regime (a) and for the transitional regime (b,c).

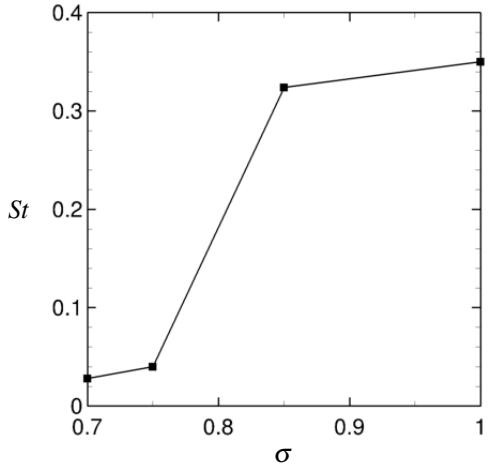

Figure 21: Value of St for different σ. Transition between cyclic and transitional regime is at $\sigma = 0.85$ approximately.

For a better understanding of this sharp jump, we perform dynamic mode decomposition (DMD) and extract the modes corresponding to the peak frequency in drag time history. We use a novel DMD algorithm developed by Anantharamu and Mahesh (2019) that has low computational cost and low memory requirements.

Figure 22 displays the mode shapes of axial velocity where it can be observed that they are substantially altered when σ is reduced from cyclic ($\sigma = 1.0$) to the transitional regime ($\sigma = 0.7$). For the transitional regime, the mode shapes are horizontally stretched and their length scale is about one order of magnitude larger than for the cyclic regime, explaining the sharp jump in shedding frequency. In addition, in the transitional regime, the near–wake of the cylinder is dominated by regions of negative velocity indicating the reverse flow due the bubbly shock propagation.

It is important to distinguish vortex shedding from cavity shedding. For cavitating flows, flow variables in the near wake can reveal both the vortex and/or cavity shedding frequency. In the cyclic regime, the dominant frequency indicates the regular shedding of a single cavitated vortex from the surface into the wake. In the transitional regime, it is observed that the growth of a cavity spanning the whole near wake region and the subsequent bubbly shock propagation, interrupts this regular vortex shedding. Consequently, an irregular and regular vortex shedding are periodically present in the cylinder wake. The dominant shedding frequency in the transitional regime indicates the cavity shedding after the passage of the condensation front and the recurrence of irregular and regular vortex shedding processes. The frequency of individual vortex shedding from the surface becomes secondary.

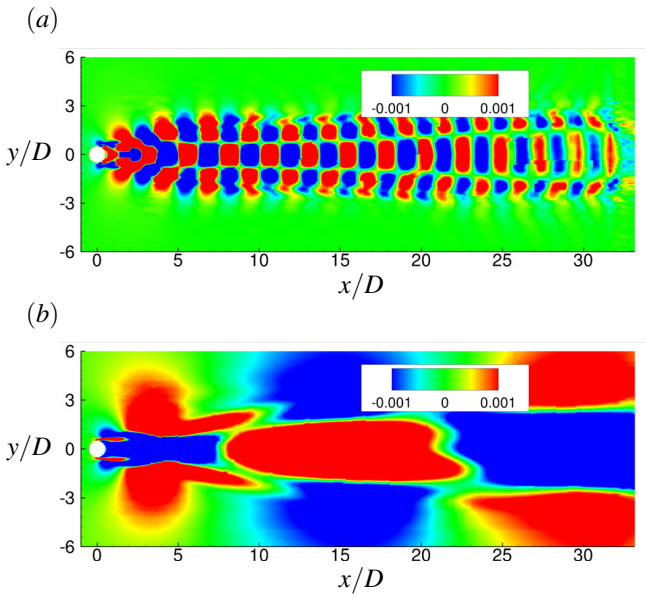

Figure 22: Modes corresponding to drag peak frequency at $\sigma = 1.0$ (a) and $\sigma = 0.7$ (b) colored by axial velocity.

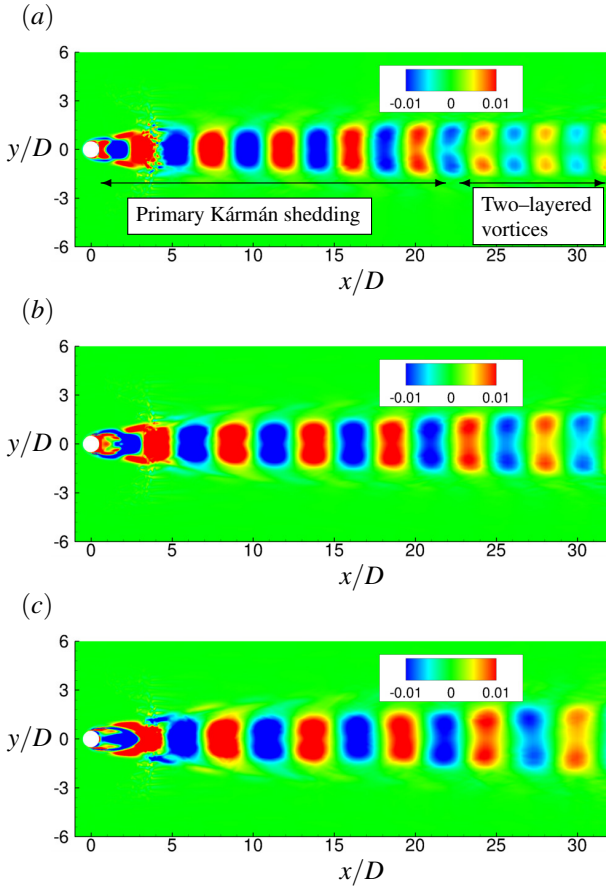

Figure 23: Most energetic modes colored by spanwise vorticity at $\sigma = 5.0$ (a), $\sigma = 1.0$ (b) and $\sigma = 0.85$ (c).

For single–phase flow over bluff bodies, the vortices shed periodically from the surface and form the classical primary Kármán vortex street in the near wake. In the intermediate wake, a transition into a two–layered vortex street is observed and its location is *Re* dependent. Durgin and Karlsson (1971) used a model in which the concentration of vorticity is strained into an elliptical shape by the nearby vortices to explain the first vortex street transition. The distorted vortex is then rotated, aligning its major axis with the streamwise direction. This process eventually results in distorted vortices merging and becoming shear layers on either side of the street. It is reported by Durgin and Karlsson (1971) that the spacing ratio, defined as the ratio between the cross–wake distance of differently signed vortices to the longitudinal distance between same sign vortices, is an important parameter that indicates the straining of the vortices and their merging. In their experiments, the authors report a spacing ratio greater than 0.366 as an indicative of the transition. In the present work, we show that this transition is delayed to further positions downstream when σ is reduced. For this, we apply DMD and extract the most dominant modes, corresponding to peak frequencies in lift time history which determine the shedding frequency of individual vortices. A non–cavitating case at $\sigma = 5.0$ is compared to the cyclic regime at $\sigma = 1.0$ and $\sigma = 0.85$. These modes are shown in figure 23 colored by spanwise vorticity.

For the non–cavitating case (figure 23(a)), the mode clearly reveal that the transition of the Kármán vortex street starts at $x = 23D$ downstream of the cylinder. A comparison with the cyclic regime shows that this transition is delayed to a position close to $x = 30D$ at $\sigma = 1.0$ (figure 23(b)) and to even farther distances at $\sigma = 0.85$ (figure 23(c)). This indicates that cavitation delays the transition of the Kármán vortex street and that its distance from the cylinder grows with decreasing σ. The vortex street is shown in figure 24(a) and 24(b) at $\sigma = 5.0$ and $\sigma = 1.0$ respectively. The vortices inside the boxes are used to compute the spacing ratio, as defined before, at two streamwise locations: the first position is the closest possible to the cylinder and the second is just before the vortex street transition. Table 1 shows that for $\sigma = 5.0$, the spacing ratio more than doubles in a short distance, surpassing the limit of 0.366 estimated by Durgin and Karlsson (1971). For $\sigma = 1.0$, however, the spacing ratio grows slower with axial distance and it is slightly higher than the threshold once the transition initiates. For the spacing ratio to be larger in the non–cavitating case, either the cross–wake distance (h) has to be higher or the longitudinal distance (a) has to be smaller. From table 1, it can be observed that it is the longitudinal distance between same sign vortices that is smaller for $\sigma = 5.0$ at the two different axial positions. This parameter is inversely proportional to the shedding

frequency of individual vortices, which is reduced from 0.193 to 0.175, based on lift history, when the cavitation number is lowered from $\sigma = 5.0$ to $\sigma = 1.0$. Thus, we can conclude that the reduction of shedding frequency due to cavitation plays a major role in delaying the first vortex street transition.

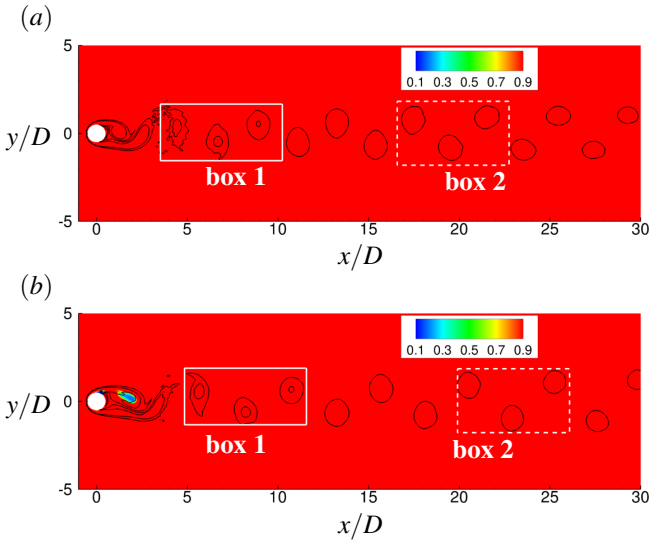

Figure 24: Vortex street colored by density for $\sigma = 5.0$ (a), $\sigma = 1.0$ (b). White boxes indicate the region where spacing ratio is computed.

For $Re = 3900$, vorticity production is investigated in the near wake for both cyclic and transitional regimes. Neglecting viscous diffusion, the vorticity transport equation reads as:

$$\frac{D\omega}{Dt} = -\omega(\nabla \cdot \mathbf{V}) + \frac{(\nabla\rho \times \nabla p)}{\rho^2} + (\omega \cdot \nabla)\mathbf{V}. \quad (8)$$

Table 1: Cross wake distance between different sign vortices (h), longitudinal distance between same sign vortices (a) and their ratio at two different wake positions for $\sigma = 5.0$ and $\sigma = 1.0$.

		h	a	h/a
$\sigma = 5.0$	box 1	0.845	4.421	0.191
	box 2	1.633	4.027	0.406
$\sigma = 1.0$	box 1	1.147	5.026	0.228
	box 2	1.751	4.724	0.371

The terms on the right–hand side of equation 8 are, respectively: vorticity dilatation, baroclinic torque and vortex stretching/tilting. Figure 25 shows instantaneous plots of the terms in equation 8 and reveals that the term most affected by the reduction in σ is the vortex stretching/tilting. This is due to the fact that in the transitional regime, a nearly two–dimensional cavity remains attached to the body during considerable part of the cycle (which can be observed by the black lines). Note that for the transitional regime, vortex stretching is only significant downstream of the cavity closure, in the intermediate wake. In addition, due to the three–dimensionality of the flow in the cyclic regime, some vorticity production is observed in the near wake due to the misalignment of density gradients and pressure gradient generated by cavity collapse. Vorticity dilatation, however, seems to increase as σ is lowered. This can be explained by the fact that by reducing σ, more vapor is generated in the near wake, increasing the compressibility of the flow.

SUMMARY

Cavitation inception is studied for two problems; shear layer of a backward–facing step and counter-rotating vortex pair interaction. For the shear layer problem, velocity profiles show very good agreement with experimental data and we confirm that elongated axial vortical structures in the shear layer are responsible for the first random sites of inception. For the vortex interaction problem, three phases of interaction have been identified based on the behavior of pressure in each core. Prior to the cores breaking apart, stretching is the main factor causing a drop in size and pressure for the secondary core and vorticity stripping is the main factor causing drop in pressure for the primary core. Post breaking apart, axial jet and local stretching of small structures occur probably causing the observed changes in secondary core pressure.

LES is used to investigate developed cavitation for two problems: flow over a wedge in the transitory and periodic regimes matching the experiments of Ganesh et al. (2016) and flow over a circular cylinder at two different *Re* and for different cavitation regimes. For the wedge problem, LES captures both the re–entrant jet and the bubbly shock wave induced sheet to cloud transition in their respective regimes. Comparison to X–ray densitometry reveals that in the developed cavitation regimes, large regions of vapor in the sheet/cloud and the resulting volume fraction field are accurately captured in the current simulations. In addition, bubbly shock propagation speed and shedding frequency show very good comparison to the experiments. For the cylinder problem, dynamic mode decomposition reveals that cavitation delays the transition of the Kármán vortex street. It also reveals that the dominant mode in the transitional regime have a length scale one order of magnitude larger than in the cyclic regime, explaining

the sharp drop in cavity shedding frequency. At high Re, we observed that vortex stretching/tilting and baroclinic torque are reduced in the near wake with decreasing σ. Vorticity dilatation, however, increases.

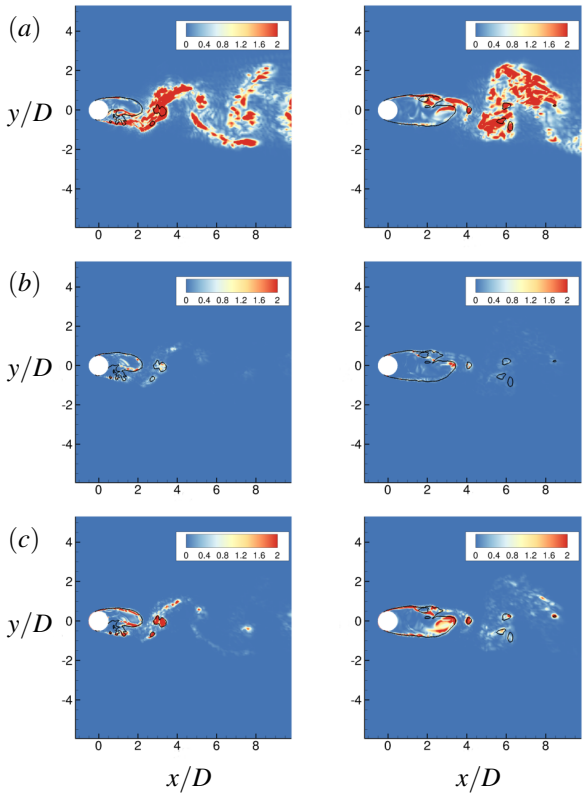

Figure 25: Vorticity transport at $\sigma = 1.0$ (left) and $\sigma = 0.7$ (right). Vortex stretching (a), baroclinic torque (b) and voriticy dilatation (c) are shown. Black lines are isolines of total void fraction of 0.1 and represent the cavity interface.

ACKNOWLEDGEMENTS

This work is supported by the United States Office of Naval Research under Grants ONR N00014–17-1–2676 and ONR N00014-14-1-0290 with Dr. Ki–Han Kim as the program manager. Computing resources were provided by the Minnesota Supercomputing Institute (MSI) and the High Performance Computing Modernization Program (HPCMP). We acknowledge Dr. Harish Ganesh and Prof. Steve Ceccio at the University of Michigan and Prof. Joseph Katz at Johns Hopkins University, for providing the experimental data. We also acknowledge Dr. Praveen Kumar for providing the recycle–rescale code and Sreevatsa Anantharamu for providing the DMD code.

REFERENCES

Agarwal, K., Ram, O., and Katz, J. "Cavitating structures at inception in turbulent shear flow". In Proceedings of the 10th International Symposium on Cavitation (CAV2018), 2018.

Anantharamu, S. and Mahesh, K. "A parallel and streaming dynamic mode decomposition algorithm with finite precision error analysis for large data". J. Comput. Phys., 380:355–377, 2019.

Arndt, R.E.A. "Cavitation in vortical flows". Annual Review of Fluid Mechanics, 74:143–175, 2002.

Bhatt, A., Wu, J., Ganesh, H., and Ceccio, S. L. "Spatially resolved x-ray void-fraction measurments of a cavitating NACA0015 hydrofoil". In Proceedings of the 32nd Symposium on Naval Hydrodynamics, Hamburg, Germany, 2018.

Bhatt, M and Mahesh, K. "Numerical investigation of partial cavitation regimes over a wedge using large eddy simulation". International Journal of Multiphase Flow, 122:103155, 2020.

Brandao, F. L., Bhatt, M., and Mahesh, K. "Numerical study of cavitation regimes in flow over a circular cylinder". J. Fluid Mech., 885:A19, 2020.

Callenaere, M., Franc, J-P., Michel, J., and Riondet, M. "The cavitation instability induced by the development of a re-entrant jet". Journal of Fluid Mechanics, 444: 223–256, 2001.

Chang, N. A., Choi, J., Yakushiji, R., and Ceccio, S. L. "Cavitation inception during the interaction of a pair of counter–rotating vortices". Physics of Fluids, 24:1–15, 2012.

Chesnakas, C. J. and Jessup, D. S. "Tip-vortex induced cavitation on a ducted propulsor". In ASME/JSME 4th Joint Fluids Summer Engineering Conference, 2003.

Durgin, W. W. and Karlsson, S. K. F. "On the phenomenon of vortex street breakdown". J. Fluid Mech., 48:507–527, 1971.

Ganesh, H., Mäkiharju, S. A., and Ceccio, S. L. "Bubbly shock propagation as a mechanism for sheet–to–cloud transition of partial cavities". J. Fluid Mech., 802: 37–78, 2016.

Ganesh, H, Deijlen, L., Bhatt, A., Wu, J., and Ceccio, S. L. "Cavitation dynamics in wakes behind bluff bodies". In Proceedings of the 32nd Symposium on Naval Hydrodynamics, Hamburg, Germany, 2018.

Gnanaskandan, A. and Mahesh, K. “A numerical method to simulate turbulent cavitating flows”. International Journal of Multiphase Flows, 70:22–34, 2015.

Hurst, N.C., Danielson, J.R., Dubin, D.H.E., and Surko, C.M. “Experimental study of the stability and dynamics of a two-dimensional ideal vortex under external strain”. J. Fluid Mech., 848:256–287, 2018.

Kumar, P. and Mahesh, K. “Towards large eddy simulation of hull–attached propeller in crashback”. In Proceedings of the 31st Symposium on Naval Hydrodynamics, California, USA, 2016.

Leweke, T, Le Dizes, S., and Williamson, C.H.K. “Dynamics and instabilities of vortex pairs”. Annual Review of Fluid Mechanics, 48:507–541, 2016.

Lund, T. S., Wu, X., and Squires, K. D. “Generation of turbulent inflow data for spatially-developing boundary layer simulations”. J. Comput. Physics, 140(2): 233–258, 1998.

Mahesh, K., Constantinescu, G., and Moin, P. “A numerical method for large-eddy simulation in complex geometries”. J. Comput. Physics, 197(1): 215–240, 2004.

Marshall, J. S., Brancher, P., and Giovannini, A. “Interaction of unequal anti-parallel vortex tubes”. J. Fluid Mech., 446:229–252, 2001.

Mitchell, G. H. G., Sampson, R., and Atlar, M. “A modern approach to the representation and use of the kca systematic propeller series”. In Third International Symposium on Marine Propulsors, 2013.

Moin, P., Squires, K., Cabot, W., and Lele, S. “A dynamic subgrid-scale model for compressible turbulence and scalar transport”. Physics of Fluids, 3(11):2746–2757, 1991.

Moore, D.W. and Saffman, P.G. “Structure of a line vortex in an imposed strain”. Aircraft Wake Turbulence and Its Detection (In: Olsen J.H., Goldburg A., Rogers M. (eds)), pages 339–354, 1971.

Muppidi, S. and Mahesh, K. “Direct numerical simulation of passive scalar transport in transverse jets”. J. Fluid Mech., 598:335–360, 2008.

O’Hern, T. J. “An experimental investigation of turbulent shear flow cavitation”. J. Fluid Mech., 215:365–391, 1990.

Saito, Y., Takami, R., Nakamori, I., and Ikohagi, T. “Numerical analysis of unsteady behavior of cloud cavitation around a NACA0015 foil.”. Comp. Mech, 40:85–96, 2007.

Schlatter, P. and Örlü, R. “Assessment of direct numerical simulation data of turbulent boundary layers”. J. Fluid Mech., 659:116–126, 2010.